Icarus 220 (2012) 730–743

Contents lists available at SciVerse ScienceDirect

Icarus

journal homepage: www.elsevier.com/locate/icarus

Constraining the size of the South Pole-Aitken basin impact

R.W.K. Potter [a,*], G.S. Collins [a], W.S. Kiefer [b,c], P.J. McGovern [b,c], D.A. Kring [b,c]

[a] Impacts and Astromaterials Research Centre, Dept. of Earth Science and Engineering, Imperial College London, London SW7 2AZ, UK
[b] Center for Lunar Science and Exploration, Lunar and Planetary Institute, 3600 Bay Area Boulevard, Houston, TX 77058, USA
[c] NASA Lunar Science Institute

ARTICLE INFO

Article history:
Received 13 October 2011
Revised 21 May 2012
Accepted 23 May 2012
Available online 13 June 2012

Keywords:
Impact processes
Cratering
Moon
Collisional physics

ABSTRACT

The South Pole-Aitken (SPA) basin is the largest and oldest definitive impact structure on the Moon. To understand how this immense basin formed, we conducted a suite of SPA-scale numerical impact simulations varying impactor size, impact velocity, and lithospheric thermal gradient. We compared our model results to observational SPA basin data to constrain a best-fit scenario for the SPA basin-forming impact. Our results show that the excavation depth-to-diameter ratio for SPA-scale impacts is constant for all impact scenarios and is consistent with analytical and geological estimates of excavation depth in smaller craters, suggesting that SPA-scale impacts follow proportional scaling. Steep near-surface thermal gradients and high internal temperatures greatly affected the basin-forming process, basin structure and impact-generated melt volume. In agreement with previous numerical studies of SPA-scale impacts, crustal material is entirely removed from the basin center which is instead occupied by a large melt pool of predominantly mantle composition. Differentiation of the melt pool is needed to be consistent with observational data. Assuming differentiation of the thick impact-generated melt sheet occurred, and using observational basin data as constraints, we find the best-fit impact scenario for the formation of the South Pole-Aitken basin to be an impact with an energy of $\sim 4 \times 10^{26}$ J (our specific model considered an impactor 170 km in diameter, striking at 10 km/s).

© 2012 Elsevier Inc. All rights reserved.

1. Introduction

The South Pole-Aitken (SPA) basin is the largest and oldest definitive impact structure on the Moon. According to widely-used crater scaling laws (e.g. Croft, 1980, 1985), the immense scale of the impact suggests normally unattainable lunar material, such as deep crust or mantle, would have been excavated or uplifted to the lunar surface, making SPA a strong candidate for possible sample return missions (National Research Council, 2007). If accessible, analysis of originally deep-seated material would aid understanding of planetary differentiation and early Solar System processes. Furthermore, samples of the impact melt produced by the SPA event would provide the geochronologic anchor needed to define the lunar basin-forming epoch and test hypotheses for the magnitude and duration of the lunar impact cataclysm.

Originally thought to be circular in shape, recent work (Garrick-Bethell and Zuber, 2009) suggests the SPA basin is elliptical with a ~1200 km semimajor axis. The basin ranges ~13 km in depth, with its lowest point at an elevation of −9.1 km (within Antoniadi crater) (Smith et al., 2010); four ring structures have been tentatively identified (Hiesinger and Head, 2003). Further analysis of the basin suggests it is in isostatic equilibrium (Zuber et al., 1994; Matsumoto et al., 2010).

Based on spectroscopic, topographic and gravity data, the basin can be divided into two zones: the Inner and Outer South Pole-Aitken Terranes (SPAT) (Jolliff et al., 2000). The Inner Terrane extends to a radial distance of ~1000 km from the basin center, over a thinner than average crust, bounded by a primary topographic depression (Jolliff et al., 2000; Garrick-Bethell and Zuber, 2009) and contains strong anomalous spectroscopic signatures. Lunar Prospector data suggests this zone has an above average Fe (8–12 wt.%: Lawrence et al., 2002) and Th (1.25–3 ppm: Lawrence et al., 2003) content; Clementine data revealed elevated Ti (1.5 wt.%: Lucey et al., 1998). Spectral data analysis has suggested the basin floor represents lower noritic crust (Pieters et al., 2001) or a mixture of lower crust and upper mantle (Lucey et al., 1998). Surface exposures of upper crustal anorthositic spectra are present, though seldom, first occurring at a radial distance of 630 km from the basin center in the rings of smaller, younger impact structures (Petro and Pieters, 2002).

The Outer Terrane begins beyond ~1000 km radius and has a thicker than average crust (Neuman et al., 1996; Jolliff et al.,

* Corresponding author. Present address: Center for Lunar Science and Exploration, Lunar and Planetary Institute, 3600 Bay Area Boulevard, Houston, TX 77058, USA.
E-mail addresses: potter@lpi.usra.edu (R.W.K. Potter), g.collins@imperial.ac.uk (G.S. Collins), kiefer@lpi.usra.edu (W.S. Kiefer), mcgovern@lpi.usra.edu (P.J. McGovern), kring@lpi.usra.edu (D.A. Kring).

0019-1035/$ - see front matter © 2012 Elsevier Inc. All rights reserved.
http://dx.doi.org/10.1016/j.icarus.2012.05.032

2000). Lunar Prospector data shows the Fe content here to be lower than the Inner Terrane (6–8 wt.%: Lawrence et al., 2002) but still above the lunar average (~5 wt.%: Lawrence et al., 2002); Th levels are comparable to the lunar average (⩽1 ppm: Lawrence et al., 2003). The edge of the Outer Terrane is marked approximately by the 5 wt.% Fe boundary at a radius of ~1200 km (Jolliff et al., 2000).

Historically, gravity coverage of the lunar farside, where SPA is located, has been limited and of low resolution. This is reflected in the range of crustal thickness estimates at the basin center: 20 km minimum (Zuber et al., 1994); 40 km (Wieczorek and Phillips, 1999); 10–30 km (Hikida and Wieczorek, 2007). Recently, however, the Kaguya mission surveyed lunar gravity and topography on both the nearside and farside at higher resolution than previous missions. These data confirm a (thin) layer, less dense than the underlying mantle, must be present under the basin center; the presence, therefore, of mantle at the surface is inconsistent with both gravity and topography data. Assuming an average crustal composition and density over the basin floor (i.e., neglecting the observed SPA compositional anomaly), data from Kaguya indicates a crustal thickness of 30 km at SPA's center, gradually thickening to 60–80 km outside of the basin (Sasaki et al., 2010; Ishihara et al., 2009); inferred crustal thickness in the inner region is therefore thinner than its surroundings and the lunar average (~50 km: Wieczorek et al., 2006). This result has been used as evidence for upper crustal material being absent in the Inner SPAT. However, given that the crust beneath the Inner SPA Terrane is of undetermined bulk composition and density, and is likely to be heavily processed by the SPA impact, the thickness of the low density layer between the mantle and the surface is uncertain. Observational evidence is therefore not consistent with mantle material being exposed at the surface inside the SPA basin.

Basin-scale crater formation is not well understood; nevertheless, scaling equations based on the reconstruction of collapsed complex craters (e.g. Croft, 1980, 1985) and the extrapolation of trends from laboratory impact experiments (e.g. Holsapple, 1993) have been used to estimate the dimensions of the transient and excavation cavities. Using a 2500 km final rim to rim diameter, Spudis (1993) and Warren et al. (1996) estimated SPA transient crater diameters of 1400 km and 1170 km, respectively. Petro and Pieters (2002) estimated a transient crater diameter of 1260 km, based on the innermost occurrences of upper crust (this would mark the outer limit of crater of excavation and therefore upper crustal removal). Laboratory-scale impact experiments and numerical impact simulations at a range of scales suggests the maximum depth of excavation (the depth of the excavation cavity) is approximately one tenth of the diameter of the transient cavity diameter. Adopting this rule for the SPA basin suggests material from a depth of approximately 120 km (well below the base of the lunar crust) should have been excavated by the SPA impact. Such deep excavation is inconsistent with observational data.

Further insight into the formation and scale of the SPA basin has come from numerical simulations of large impacts on the Moon (Collins and Melosh, 2004; Ivanov, 2007; Hammond et al., 2009; Ivanov et al., 2010; Schultz and Crawford, 2011). Although none of these models were compared rigorously with observational constraints, all concluded a SPA basin-forming impact would have exhumed mantle material to the lunar surface either through excavation or as part of the central uplift collapse. These numerical models also predicted the formation of a large melt pool, underlying the inner basin, consisting of molten mantle and, perhaps, lower crust. If a melt pool did form under the basin then it is likely to have been large enough to undergo differentiation (Morrison, 1998; Cintala and Grieve, 1998). A cooling melt mixture derived from mantle and lower crustal material would initially produce olivine, which would settle out, driving the remaining melt to noritic compositions (e.g. Morrison, 1998). This differentiation process would have produced near-surface lithologies that may not reflect those of the mantle, therefore making it difficult to ascertain whether pure mantle material had been excavated.

A working hypothesis synthesizing both observational data and numerical modeling is, therefore, that the SPA impact excavated the majority (if not all) of the lunar crust, generating a large central melt pool of predominantly molten mantle. This melt pool then differentiated, cooled and re-crystallized to leave a low density surface layer with a composition intermediate to that of pure lower crust and pure mantle (similar to that observed by spectroscopic data). If this hypothesis is correct, the dimensions of the compositional anomaly in the SPA basin and gravity data provide constraints on the dimensions and shape of the melt pool and surrounding variations in crustal thickness. Here, we describe new hydrocode simulations of SPA-scale impacts and compare predictions of the volume, dimensions and final location of the melt pool and crustal deformation with observational constraints. The aim of this study is to determine the size and magnitude of the SPA impact, under the assumption that the above working hypothesis is correct. As one of the unknowns in simulating the SPA impact is the thermal state of the Moon at the time of impact, we investigate the effect of thermal gradient (as well as impactor size) on final basin structure and melt volume. From our best-fit model we provide constraints on the fate and evolution of mantle material in the SPA impact.

2. Methods

The two-dimensional iSALE hydrocode (Amsden et al., 1980; Collins et al., 2004; Wünnemann et al., 2006) was used to numerically model SPA-scale impacts. iSALE has previously been used to model mid- and large-scale terrestrial impacts including: Chicxulub (Collins et al., 2008b); Ries (Wünnemann et al., 2005); Chesapeake (Collins and Wünnemann, 2005) and Haughton (Collins et al., 2008a) and is well tested against other hydrocodes (Pierazzo et al., 2008) and laboratory experiments at both high and low strain-rates (Wünnemann et al., 2006).

The most probable impact angle is 45° to the horizontal (Shoemaker, 1962) and the SPA basin is thought to have been formed by an oblique impact (⩽ 30°: Schultz, 1997) due to its elliptical shape (Garrick-Bethell and Zuber, 2009). Oblique impacts differ in several ways to near-vertical impacts; for example, transient crater size and melt volume is reduced in an oblique impact relative to a vertical impact (Pierazzo and Melosh, 2000b). Moreover, crater shape and ejecta distribution can become significantly asymmetric at low impact angles. Consequently, a 3D hydrocode, which can simulate impacts at oblique angles, would in some ways be the preferred numerical approach for modeling SPA. However, as 3D simulations carry a high computational cost, 2D simulations still have the considerable advantage that they can be performed at substantially higher resolution than 3D simulations and therefore provide a more accurate representation of vertical impacts.

In addition, in their numerical studies of melt production in oblique impacts, both Pierazzo and Melosh (2000b) and Marinova et al. (2011) found the ratio of melt volume-to-transient crater volume remained fairly constant for impact angles greater than 15°. This implies, in the case of impact melt production at least, the consequences of vertical impacts are qualitatively similar to those of an oblique impact. Though 2D simulations of vertical impacts are an idealized representation of an impact that will not replicate any asymmetry in crater formation, it is expected that axisymmetric 2D simulations of crater formation will produce the correct azimuthally averaged behavior.

To investigate SPA-scale impact scenarios on the Moon we simulated vertical impacts of asteroids 100–250 km in diameter at

velocities of 10–35 km/s, into a 'Moon-like' target. A cell size of 2.5–5 km per cell (resulting in 10–34 cells per projectile radius, CPPR) was used. The Moon-like target was modeled as a three-layer sphere, 1750 km in radius (slightly larger than the Moon's true radius of 1737 km), consisting of a 50 km thick crust (taken as the average lunar crustal thickness (Wieczorek et al., 2006), a 1350 km thick mantle and a 350 km radius core. ANEOS-derived equation of states for dunite (Benz et al., 1989) and iron (Thompson and Lauson, 1972) were used to represent the mantle and core response to thermodynamic changes and compressibility. As an ANEOS equation of state for lunar crustal material was not available, we used the Tillotson equation of state (Tillotson, 1962), with parameters determined for gabbroic anorthosite (O'Keefe and Ahrens, 1982), to model the thermodynamic response of crustal materials to impact. The Tillotson equation of state as implemented in iSALE includes only an approximate estimate of temperature (Ivanov et al., 2002) and a rudimentary treatment of vaporization (see Melosh (1989) Appendix II, for details). However, as the highly shocked crust inside the basin is entirely removed during the impacts we simulated and vapor production was not our focus, the accuracy of the equation of state used for the crust was not critical. Simulations using alternative equations of state for the crust did not produce significantly different results to those presented here.

In addition to the mantle, dunite was also used to represent the impacting asteroid as it is a useful proxy for asteroidal material (Pierazzo et al., 1998; Pierazzo and Melosh, 2000a); the normal density of dunite was used as we assume large basin-forming objects would not be significantly porous. The amount of vapor production was not important in this work, and therefore to decrease computation time, material with a density less than 0.5% of the appropriate reference density was removed from the calculations.

Self-consistent pressure, gravity and density fields were computed based on a prescribed temperature versus depth profile within the Moon, approximating lunar conditions at the time of the SPA impact. The temperature profiles comprised a near-surface conductive heat-transfer portion, described by a quadratic temperature-depth relationship, and a convective portion at depth. Based on studies of lunar elastic thickness (Solomon and Head, 1980; Crosby and McKenzie, 2005) temperature gradients between 10 K/km and 50 K/km were considered plausible (Fig. 1). Using these gradients a lithospheric thickness was calculated and a smoothing function applied to transition between the conductive and convective portions at the base of the lithosphere. The temperature profiles were bounded by the solidus so that, at any location, mantle temperatures never exceeded the mantle solidus. In reality, lower lithospheric/upper asthenospheric temperatures may exceed the solidus, however results showed melt volume was primarily affected by impact size (magnitude) and the near surface thermal gradient rather than lower lithospheric/upper asthenospheric temperatures. In the convective portion of the temperature profile, an adiabatic temperature gradient was assumed, pinned to a temperature of 1723 K (1450 °C) at a depth of 560 km, based on thermal evolution studies (Spohn et al., 2001; Ghods and Arkani-Hamed, 2007). Although our assumed deep mantle adiabat is quite consistent with estimates of early lunar temperatures in the literature (Spohn et al., 2001; Ghods and Arkani-Hamed, 2007; Ziethe et al., 2009), other deep mantle temperature profiles are possible and should be investigated in future work. Because our assumed temperature profiles vary only in the conductive portion, the temperature profiles are henceforth referred to as lithospheric thermal gradients (LTGs). At the start of the calculation, the gravity field was computed to be consistent with the internal density distribution within the modeled Moon and to decay with reciprocal distance from the surface squared. This gravity field was not updated during the simulation.

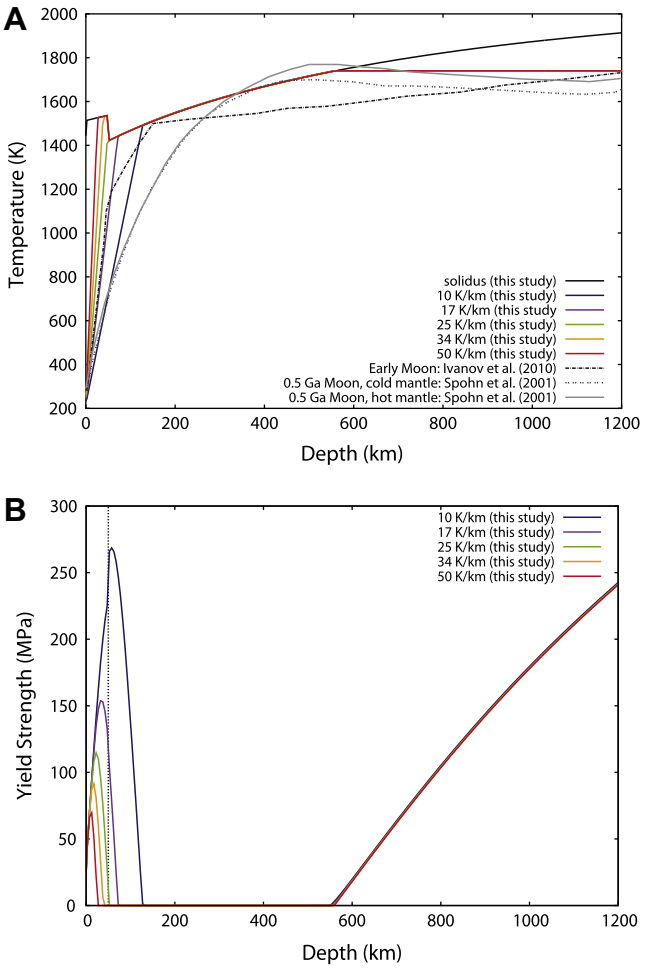

Fig. 1. (A) Temperature and (B) yield strength within the crust and upper mantle for the various lithospheric temperature gradients (LTGs) investigated. Temperatures are bounded by the mantle solidus. Early Moon temperature profiles from Ivanov et al. (2010) and Spohn et al. (2001) are included for comparison; the Spohn et al. (2001) curves represent a 0.5 Ga Moon with an initially 'hot' and 'cold' mantle. The dotted line in (B) represents the boundary between the crust and mantle.

To simulate the large-scale final basin structure it is necessary to account for the strength and rheology of the early Moon, which become important in the late stages of crater formation. Of the various influences on target strength, the most significant for giant impact basin formation is the dependence of strength on pressure and temperature (Ivanov et al., 2010). In this work, the shear strength model of Collins et al. (2004) was used to represent the resistance of the impactor and the Moon target to shear deformation. Strength and thermal model parameters (e.g. yield strength, melt temperature) for the crust material were calculated from fits to experimental gabbro rock strength data (Azmon, 1967; Stesky et al., 1974; Shimada et al., 1983). For the impactor and mantle material, model parameters were derived from fits to both dunite (Shimada et al., 1983; Ismail and Murrell, 1990) and peridotite data (Stesky et al., 1974; McKenzie and Bickle, 1988). See Table 1 for calculated crustal and mantle parameters.

Due to the high internal temperature of the Moon assumed in our simulations, the effect of temperature on strength is of particular importance. Geological materials lose strength as their temperature increases; all shear strength is lost upon melting (e.g. Jaeger and Cook, 1969). In iSALE, this relation is approximated by the equation (after Ohnaka, 1995)

$$Y_t/Y = \tanh[\xi(T_m/T) - 1] \quad (1)$$

Table 1
Calculated strength and thermal parameters used to represent the lunar crust and mantle. μ_d and μ_i are the coefficients of friction for damaged and intact rock respectively, Y_o and Y_m are material strength parameters, ξ, a and c are material constants, and T_m is the solidus.

Parameter	Crust	Mantle
μ_d	0.71	0.63
μ_i	1.1	1.58
Y_o (Pa)	3.19×10^7	5.07×10^6
Y_m (Pa)	2.49×10^9	3.26×10^9
ξ	1.2	1.1
a (Pa)	1.84×10^9	1.52×10^9[a]
c	7.27	4.05[a]
T_m (K)	1513	1373[a]

[a] Data taken from Davison et al. (2010).

where Y_t is the material's thermally-weakened yield strength, Y is material strength at low temperature, T is ambient temperature, ξ is a material constant and T_m is the solidus, calculated using the Simon approximation:

$$T_m = T_0(P/a + 1)^{1/c} \quad (2)$$

where T_m is the solidus temperature at pressure P, T_0 is the solidus at normal pressure, and a and c are material constants found by fitting this equation to experimentally-derived melting data for peridotite (McKenzie and Bickle, 1988).

As the ambient temperature approaches the solidus temperature in Eq. (1) the bracket on the right-hand side tends to zero, thus material strength drops to zero. Hence, according to this model, any material above the solidus offers no resistance to shear. Fig. 1B illustrates how strength varied within the crust and upper mantle of our Moon target for our chosen LTGs. In the shallowest LTG (10 K/km) target strength drops to zero at a depth of ~130 km, in the steepest LTG (50 K/km) it reaches zero at ~30 km. Our modeled Moon therefore consists of a relatively thin, brittle and strong lithosphere on top of a very weak asthenosphere. A consequence of the relative proximity of this weak material to the lunar surface is that for impacts on the scale of the SPA basin, the material underlying the crater floor is weak enough to permit wholesale crater collapse by virtue of its high temperature alone. In other words, additional target weakening mechanisms, such as acoustic fluidization (Melosh, 1979; Melosh and Ivanov, 1999), which are often invoked to explain the collapse of complex craters much smaller than the SPA basin (e.g. Wünnemann and Ivanov, 2003), appear not to be required to facilitate collapse of SPA. Test simulations including the effect of acoustic fluidization (i.e., the block-model approximation (Melosh and Ivanov, 1999; Wünnemann and Ivanov, 2003)) did not alter the results and for simplicity we did not apply any acoustic fluidization model in the simulations presented here.

While a complete loss of resistance to shear upon melting is true for geological materials at low strain rates, the rheology of partially molten material during the high strain rates of an impact is more complicated (Stewart, 2011). It is likely that the multiphase mixture of solid and melt will offer considerable resistance to deformation, which may be rate-dependent, pressure-dependent, or both. In this work, we accounted for the resistance of super-solidus material by assuming a constant partial melt viscosity of 10^{10} Pa s. Although this approach is an undoubted oversimplification, it serves as a useful first approximation for future improvement.

The volume of mantle melt resulting from the impact was quantified using a method similar to that of Ivanov et al. (2010). Massless tracer particles, initially placed one per grid cell (for all but one simulation the cell size was 5 km), tracked the path followed by the material that began in that cell. Throughout the simulation the temperature and pressure at the location of the tracer was recorded. In post-processing, the pressure of the tracer at any given time was used to calculate the instantaneous melt temperature of the material tracked by the tracer using the Simon approximation. If the temperature recorded by the same tracer at the same time exceeded the instantaneous liquidus melt temperature, the mass associated with the tracer was defined as completely molten at that time: in this case the volume of material represented by the tracer was added to the total melt volume. On the other hand, if the tracer temperature exceeded the solidus temperature but was less than the liquidus temperature, the tracer was defined as partially molten: in this case, the volume of melt that was added to the total was a fraction of the volume of material represented by the tracer, which was assumed to vary on a linear scale between 0 at the solidus to 1 (completely molten) at the liquidus. We note that internal pressure fluctuations in the Moon, generated by shock wave reflections and surface waves, cause the instantaneous melt temperature (as predicted by the Simon approximation) to oscillate dramatically during the simulation. As a result, it was necessary to calculate the total mantle melt volume after the major cratering motions had ceased and the internal pressure fluctuations had attenuated significantly. Only those tracers that were in a (partially) molten state at late times contributed to the total melt volume.

One disadvantage of using ANEOS equation of state tables is that they do not account for the latent heat of melting. Temperatures in excess of the solidus are therefore over estimated and result in unrealistically large melt volumes. In light of this problem, we include a correction for latent heat in our melt volume calculations. As stated above, we assume melt production increases linearly with temperature between the solidus and liquidus. Therefore the latent heat of melting would be absorbed uniformly with temperature between the solidus and liquidus. With this assumption, the effect of latent heat can be accounted for by using an enhanced heat capacity $\left(C_p'\right)$ when the temperature is between the solidus and liquidus, $C_p' = C_p + L/(T_L - T_S)$ (Onorato et al., 1978), where C_p is the heat capacity, L is the latent heat, T_L is the liquidus and T_S is the solidus. A similar correction process is used to calculate adiabatic decompression melting in convecting systems (Langmuir et al., 1992; Kiefer, 2003). We adopt characteristic values of C_p = 1300 J/kg K and L = 700,000 J/kg based on the compilation of Navrotsky (1995) assuming a mantle that is dominated by olivine and pyroxene. Neglecting this latent heat correction would result in melt volumes that are about a factor of 4 larger than they actually are. All melt volumes quoted in the remainder of this paper take into account this correction for latent heat.

Due to the nature of the cratering process for large-scale impacts, and our use of a pressure-dependent melt criterion, the mantle melt volume includes mantle material (partially) melted by decompression as well as by shock heating. Decompression melting results from material being uplifted from a deep, high-pressure location to a shallower, less-pressurized location. The decrease in pressure lowers the ambient melt temperature, which may permit melting if the temperature of the uplifted material remains high. In general, decompression melting is not regarded as an important aspect of the impact process because of the relatively cold state of planetary lithospheres (Ivanov and Melosh, 2003). However, as decompression melting can be important in very large impacts and/or in impacts into regions with high temperature gradients (Jones et al., 2002), its effects are important to consider when simulating SPA-scale basins that formed while the Moon was hot.

3. Results and discussion

3.1. The basin-forming process

Fig. 2 illustrates the impact basin-forming process, as predicted by our numerical simulations. The evolution of the crater is similar

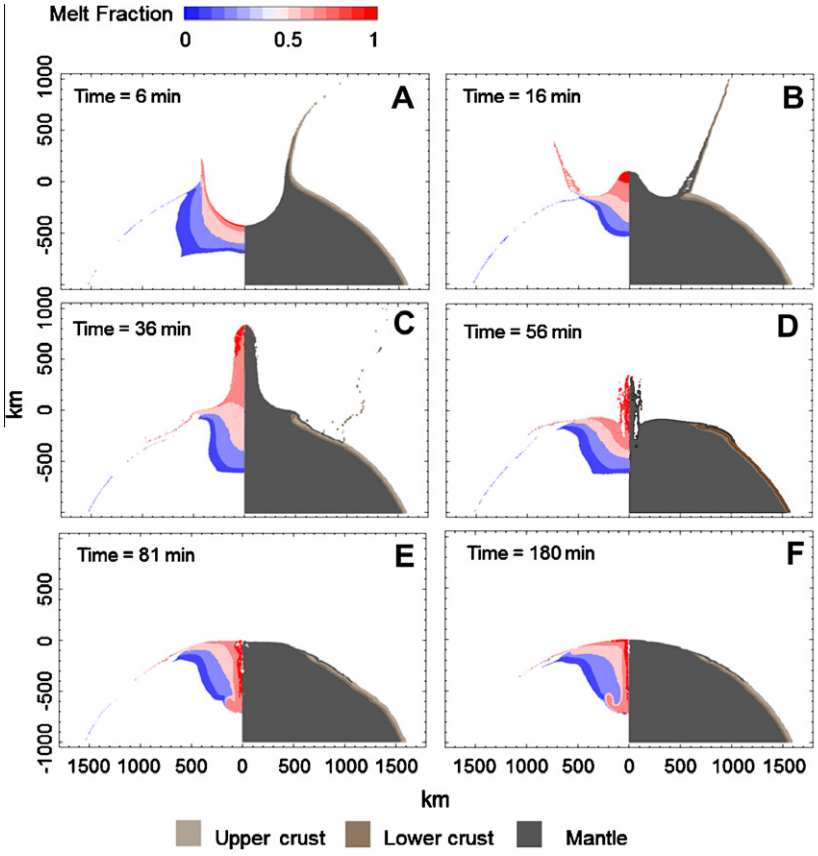

Fig. 2. The basin-forming process. Each plot (A–F) shows crustal and mantle material in the right panel and the distribution and fraction of mantle melt in the left panel; vapor is removed from the simulations and is not plotted here. See text for description.

to the planetary basin-forming impacts described in Ivanov et al. (2010) and models proposed for the Chicxulub impact (Collins et al., 2002, 2008b) and other large craters (O'Keefe and Ahrens, 1999). Compared to the Chicxulub models, the basin-forming process here is on a much larger scale and is facilitated by a thermally softened lunar subsurface. The impact creates a large bowl-shaped cavity as material is excavated and displaced from the impact site (Fig. 2A). During this stage, the crust inside the cavity and some mantle material is ejected ballistically, landing well outside the cavity. Prior to the cavity reaching its maximum lateral extent of excavation, the crater floor begins to rise, forming a central uplift (Fig. 2B). The central uplift, weakened by the residual heat from the impact, rises well above the pre-impact surface (Fig. 2C). The height of the uplift is to some degree exaggerated by flow convergence on the central axis boundary condition; uplift is likely to be less prominent in oblique impacts. The uplift then collapses back downwards and outwards interacting with crater wall and some proximal ejecta blanket material which is collapsing inward towards the basin center (Fig. 2D). This complex interaction deforms the crust outside the crater and pushes mantle material out and on-top-of the crust outside the cavity. Further oscillations of the central region produce secondary uplift and collapse phases that eventually attenuate as energy dissipates (Fig. 2E). The oscillations generate a series of surface waves that deform the crust surrounding the melt pool before attenuating into seismic waves that propagate around the Moon.

After the major cratering motions have ceased, the final basin is composed of a large central pool of molten mantle where all crustal material has been removed (Fig. 2F). In general, melt fraction decreases with depth and with radial distance from the crater center. Farther out, mantle material excavated during initial cavity growth or exhumed by the outward collapsing central uplift overlays crustal material, which gradually thickens away from the impact site. The simulated distribution of molten material away from the symmetry axis (radius > 100 km) and above 500 km depth is robust, but the deep central plume of high melt fraction material is not. This plume is formed by flow convergence on the central axis boundary that is peculiar to vertical impact and may not be captured correctly by a cylindrical-geometry model; three-dimensional simulations of oblique impact would likely not produce this deep central plume. In our models, the depth of this plume is sensitive to impact velocity and the viscosity of the partially molten material.

The major cratering motions and processes described above are qualitatively similar for the range of impactor and target conditions simulated; videos of some SPA-scale simulations can be found here (link to Video 1, Video 2 and Video 3). Below we describe the sensitivity of melt production, crater excavation and final crustal structure around the crater to impact energy and lithospheric temperature gradient (LTG) (see Table 2 for simulation comparison)

.

3.2. Transient crater size and maximum depth of excavation

Popular concepts in impact cratering are the transient crater or transient cavity, which is the form of the crater at the end of excavation and prior to subsequent gravitational collapse (Dence, 1965), and the excavation cavity, which marks the boundary between the impacted material that is ejected out of the crater and the material that is displaced but remains in the crater. The radius of both the excavation and transient cavity represents the

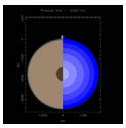

videos of some SPA-scale simulations can be found in the supplementary online material (see Appendix A).

videos of some SPA-scale simulations can be found in the supplementary online material (see Appendix A).

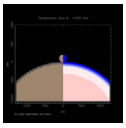

videos of some SPA-scale simulations can be found in the supplementary online material (see Appendix A).

maximum radius at which material is ejected outward from the crater. The depth of the transient cavity is the maximum depth achieved by the growing crater, while the excavation (cavity) depth is defined by the deepest material to be ejected from the crater. In small craters, the shape and size of the transient crater can be determined from observations, which suggest the depth-to-diameter ratio of the transient crater is approximately constant, regardless of the crater size (Croft, 1985). Moreover, numerical and laboratory experiments have shown that (for small craters) transient crater volume and diameter can be used to predict (with reasonable accuracy) the energy and momentum of the impact (Holsapple, 1982; Schmidt and Housen, 1987), the volume of impact melt (Grieve and Cintala, 1992) and the maximum depth and volume of ejected material (the depth and volume of the excavation cavity), using simple scaling laws.

However, the transient and excavation cavities are not clearly defined concepts in large (basin)-scale crater formation. Numerical models (e.g. Turtle et al., 2005) of large crater formation have shown the crater floor begins to uplift prior to the cavity reaching its maximum lateral extent. As a result, the maximum cavity depth is achieved before the maximum radius of ejection and the crater never takes the canonical form of a paraboloid of revolution with a 1:3 transient depth-to-diameter ratio. In addition, the collapse stage of the cratering process is so extensive that a large portion of the proximal ejecta and the uplifted cavity rim slump into the crater, terminating inside the final crater rim. The ejecta blanket surrounding the final crater rim will contain a mixture of material from a variety of depths, however the majority of ejecta derived from the greatest depth in the target will be found among the most proximal ejecta which slumps back into the crater.

Despite the transient and excavation cavities not being clearly defined in large-scale crate formation, it is nevertheless useful to extract from numerical simulations information that constrains the size of the crater at the approximate transition of excavation and collapse. For this study, we defined the transient crater volume as the maximum crater volume and the transient crater radius as the radius of the crater at this same instant. This is consistent with the definition of the transient crater in small craters and is easy to measure from our simulations. It is worth noting, however, that the time of maximum crater volume occurs after the crater floor begins to uplift and so does not coincide with the time of maximum crater depth.

Model results of transient crater size are presented in Fig. 3, where a non-dimensional measure of crater diameter, Π_D, defined as

$$\Pi_D = D_{tc}/(M_{proj}/\rho)^{1/3} \quad (3)$$

where D_{tc} is the transient crater diameter, M_{proj} is the mass of the projectile, and ρ is the target density (we use the mantle density 3314 kg/m^3 as the entire crust is removed during the simulations), is plotted against the gravity-scaled impact size, Π_2, defined as

$$\Pi_2 = 3.22ga/u^2 \quad (4)$$

Table 2
Model data for all impact simulations at 10 km/s. LTG: lithospheric thermal gradient, D_i: impactor diameter, D_{tc}: transient crater diameter, V_m: melt volume. V_{tc}: transient crater volume, Z_{ex}: maximum excavation depth, Π_2 and Π_D: dimensionless impact parameters. All simulations were run using a cell size of 5 km, apart from the high resolution best-fit run (italicized in the table), which was run using a cell size of 2.5 km.

LTG	D_i (km)	D_{tc} (km)	V_m (10^8 km^3)	V_{tc} (10^8 km^3)	V_m/V_{tc}	Z_{ex} (km)	Z_{ex}/D_{tc}	Π_2 (10^{-3})	Π_D
50	250	1139	2.25	3.22	0.70	137.5	0.12	6.48	5.65
50	220	1032	1.49	2.30	0.65	122.5	0.12	5.70	5.82
50	200	929	1.10	1.80	0.61	112.5	0.12	5.18	5.76
50	170	819	0.67	1.17	0.55	97.5	0.12	4.41	5.98
50	*170*	*837*	*0.69*	*1.27*	*0.57*	*101.25*	*0.12*	*4.41*	*6.11*
50	150	722	0.42	0.85	0.50	87.5	0.12	3.89	5.97
34	250	1140	2.18	3.20	0.68	137.5	0.12	6.48	5.82
34	220	1032	1.43	2.30	0.62	122.5	0.12	5.70	5.82
34	200	928	1.07	1.79	0.60	112.5	0.12	5.18	5.76
34	180	855	0.77	1.35	0.57	102.5	0.12	4.67	5.89
34	150	717	0.45	0.85	0.53	87.5	0.12	3.89	5.93
25	250	1138	2.05	3.21	0.64	137.5	0.12	6.48	5.65
25	220	1029	1.42	2.29	0.62	122.5	0.12	5.70	5.80
25	200	925	1.05	1.79	0.59	112.5	0.12	5.18	5.74
25	180	850	0.80	1.35	0.59	97.5	0.11	4.67	5.86
25	150	714	0.42	0.85	0.49	82.5	0.12	3.89	5.90
25	100	500	0.10	0.28	0.37	57.5	0.11	2.59	6.20
17	200	919	0.97	1.78	0.55	107.5	0.12	5.18	5.70
17	170	803	0.59	1.15	0.51	97.5	0.12	4.41	5.86
17	150	708	0.40	0.84	0.47	87.5	0.12	3.89	5.86
10	200	878	0.82	1.73	0.47	112.5	0.13	5.18	5.45
10	170	734	0.47	1.10	0.43	97.5	0.13	4.41	5.36
10	150	662	0.31	0.79	0.40	87.5	0.13	3.89	5.48

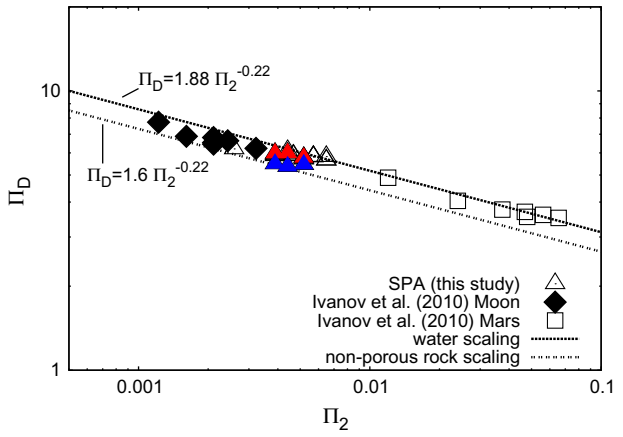

Fig. 3. Model results, this study and that of Ivanov et al. (2010), and water and non-porous rock scaling laws (Schmidt and Housen, 1987), for Π_D, a measure of transient crater size, against Π_2, a gravity-scaled impact size. Our model results agree favorably with the Moon models of Ivanov et al. (2010). The red and blue triangles highlight comparable model results in the steepest and shallowest LTGs, respectively, in this SPA study. Equations for the water and non-porous rock scaling laws are given in the figure.

where g is gravitational acceleration, a is the impactor radius, and u the impact velocity. Our results (triangles) compare favorably with the lunar basin-forming models of Ivanov et al. (2010) (diamonds), plotting between the scaling laws for water and non-porous rock. For a given impact scenario (a constant Π_2), the steeper the LTG, the larger the value of Π_D. The model results suggest impacts into the steeper LTGs follow the scaling for water, whilst impacts into the shallowest LTG follow the non-porous rock scaling. This is not surprising, as the warmer LTG's have a lower near-surface strength, allowing a given impact energy to create a larger transient crater.

The maximum depth of excavation was also extracted from our simulation results. In this work we assumed that the transient and excavation cavities have the same diameter and defined the maximum depth of excavation by locating the deepest material ejected from the transient crater during excavation. As the crater rim cannot easily be extracted from our data, we cannot relate accurately the ultimate position of excavated material to the final crater rim. However, we emphasize that according to our definition of ejected material, the deepest ejecta lands inside the final crater rim. Our simulation results show maximum excavation depth is a constant fraction of transient crater diameter, with a ratio of 0.12 ± 0.01 for all modeled impact scenarios (Fig. 4). This agrees well with previous experimental, analytical, geological and geophysical investigations of impact craters of all sizes which suggest an excavation depth-to-diameter range of 0.08–0.12 (Croft, 1980; Melosh, 1989; Spudis, 1993; Wieczorek and Phillips, 1999; Hikida and Wieczorek, 2007). Previous SPA-scale modeling by Hammond et al. (2009) suggested excavation depth-to-diameter ratios of 0.17 ± 0.03 for basins 500–2600 km in diameter.

Wieczorek and Phillips (1999) and Hikida and Wieczorek (2007) suggested three of the largest lunar basins: Imbrium, Serenitatis and SPA, had far lower excavation depth-to-diameter ratios ($\ll$0.1) compared to other, smaller basins ($\sim$0.1) implying some kind of non-proportional scaling. They came to this conclusion by estimating excavation cavity size through geometrically restoring inferred basin crustal profiles to pre-impact states. However this method assumed there was negligible lateral translation of basin material during formation; the results presented here show lateral translation of material is extensive (see Fig. 2), invalidating the assumption of the reconstruction models. As our excavation depth-to-diameter ratios agree well with previous experimental, analytical, geological and geophysical investigations of craters at all sizes, this suggests SPA-scale impacts follow proportional scaling, and that the reconstruction method of Wieczorek and Phillips (1999) and Hikida and Wieczorek (2007) is too simplistic to estimate excavation cavities for the largest lunar impacts.

The maximum excavation depth achieved in all our models was far less than the maximum cavity depth; the transient cavity and the excavation cavity are not synonymous. This is consistent with previous computational and experimental data suggesting the excavation depth is approximately one third of maximum cavity depth (Melosh, 1989).

3.3. Impact-generated mantle melt production

Our models create a large, central (partially molten) mantle melt zone around the basin center, consistent with previous

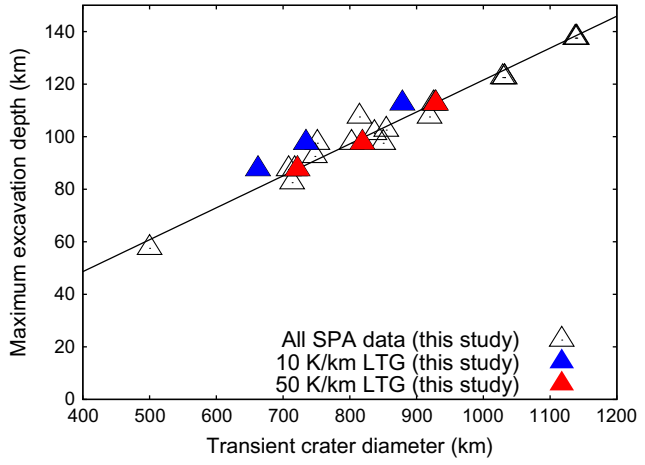

Fig. 4. Maximum excavation depth for a number of modeled impacts against transient crater diameter. Excavation depth-to-diameter ratio remains consistent ($\sim$0.12) for impacts of all sizes into the different LTGs. The red and blue triangles highlight comparable impacts into the steepest and shallowest LTG. Maximum excavation depth for a given impact in the steepest and shallowest LTG is the same (to within 5 km), while the transient crater is larger in the steeper LTG, as a result of lower target strength.

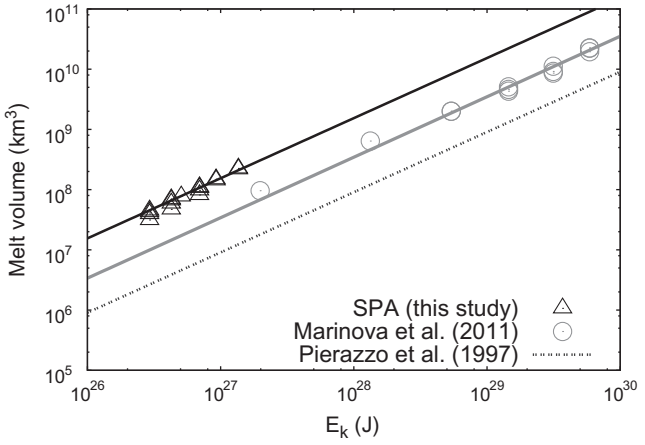

Fig. 5. Impact-generated melt volume plotted against impact energy (E_k). Calculated SPA melt volumes, corrected for latent heat (black triangles), are plotted along with melt volumes from planetary-scale impacts (Marinova et al., 2011) and a scaling study (Pierazzo et al., 1997). Fits to these data are $1.7 \times 10^{-19} E_k$ (solid black line – this SPA study); $2.6 \times 10^{-20} E_k$ (solid gray line – Marinova et al., 2011) and $9.6 \times 10^{-21} E_k$ (Pierazzo et al., 1997).

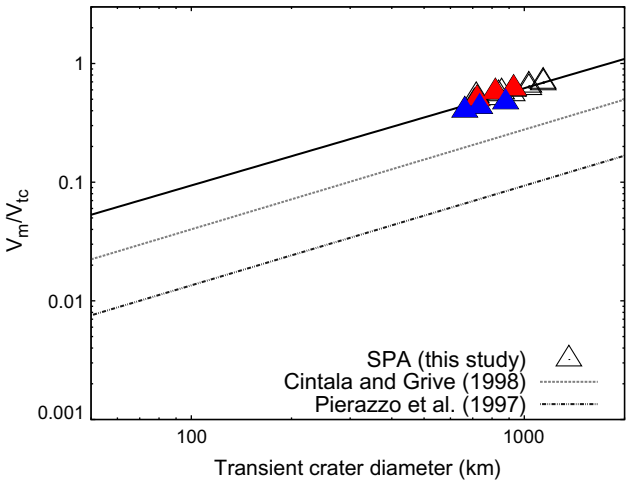

Fig. 6. The ratio of melt volume to transient crater volume (V_m/V_{tc}) plotted against transient crater diameter. Along with our SPA results are scaling laws from Cintala and Grieve (1998) and Pierazzo et al. (1997). Fits to these data are 0.0022 $Dtc^{0.82}$ (solid black line – this SPA study); 0.00083 $D_{tc}^{0.84}$ (Cintala and Grieve, 1998) and 0.00028 $D_{tc}^{0.84}$ (Pierazzo et al., 1997). The red and blue triangles compare SPA simulations using the steepest and shallowest LTGs, respectively.

numerical models of SPA-scale impacts (Collins and Melosh, 2004; Ivanov, 2007; Hammond et al., 2009; Ivanov et al., 2010). This material is emplaced around the basin center as a result of crustal excavation and the rise and collapse of the central uplift, bringing originally deep-seated mantle material towards the lunar surface. This zone is bounded by an annulus of crustal material. A second, outer, zone of (molten and unmolten) mantle is found overlying crustal material. This mantle material is primarily excavated: excavated mantle located farther away from the basin center originated closer to the basin center, while excavated mantle found just beyond the extent of the transient crater originated from just within the transient crater. However the ultimate location of this mantle material is affected by the collapsing uplift, which forces the mantle material further away from the basin center.

Fig. 5 illustrates how melt volume varies with impact energy. The SPA melt volumes (with the correction for latent heat) plot noticeably above the planetary-scale impacts of Marinova et al. (2011) which in turn plot above the scaling law from Pierazzo et al. (1997). Prior to impact, the temperature within the target is cold (room temperature) and uniform in the Pierazzo et al. (1997) study, while in Marinova et al. (2011) and this study, temperature increases with depth within the target. This explains the lower melt volume estimates of Pierazzo et al. (1997); a cold, uniform temperature target will require a greater amount of energy to melt than a pre-heated target. The melt volumes of both Marinova et al. (2011) and Pierazzo et al. (1997) represent complete melt, that is material with temperatures in excess of the liquidus. These are therefore underestimations of the total melt volume as material with a temperature between the solidus and liquidus will contain some molten material. We take this into account in our SPA simulations, by including a fractional melt calculation between the solidus and liquidus as well as including the volume above the liquidus, hence our larger melt volumes. Our parameter space does not overlap that of Marinova et al. (2011), however our data imply a greater volume of melt for the range of impact energies explored by Marinova et al. (2011). This is to be expected as we include the fractional melt calculation. Another difference could be due to the equation of states used; in this study we used an ANEOS equation of state for mantle whereas Marinova et al. (2011) used a Tillotson equation of state for the mantle.

Fig. 6 plots the ratio of melt volume to transient crater volume against transient crater diameter. Our results show SPA-scale impacts produce a melt volume 50–70% of the transient crater volume. This is a far greater fraction than that predicted by scaling laws. The Cintala and Grieve (1998) scaling law assumes a chondrite impactor (density = 3580 kg/m^3), anorthosite target (density = 2940 kg/m^3), and a 10 km/s impact, while the Pierazzo et al. (1997) scaling law assumes a dunite impactor and target (density = 3300 kg/m^3), an impact velocity of 10 km/s and that only material with temperatures above the liquidus is molten, hence their different values. However, both assume a cold, uniform temperature target, and this is the likely reason why our SPA data plots well above these scaling laws. Our results suggest an impact producing a transient crater ~2000 km in diameter, comparable to the radius of the Moon will produce a volume of melt equivalent to its transient crater volume. Highlighted in Fig. 6 are two sets of impacts using the steepest/warmest (red triangles) and shallowest/coolest (blue triangles) lithospheric thermal gradients (LTGs). Each set contains impactors 150, 170, and 200 km in diameter. For a given impactor diameter (and therefore impact energy), impacts into the steeper LTG produce a greater transient crater diameter and a greater melt volume to transient crater volume than the corresponding impact into the shallowest LTG. This is because the steepest LTG target is relatively weaker allowing the formation of a larger transient crater. The initially warmer conditions

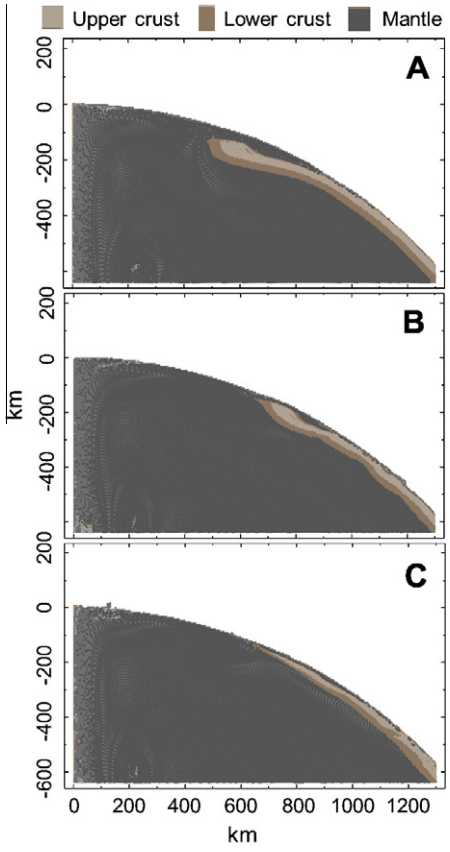

Fig. 7. The effect of differing LTGs (a) 10, (b) 25, and (c) 50 K/km on the distribution of crustal and mantle material following the impact of a 200 km impactor at 10 km/s. Crustal material (beige – upper crust; brown – lower crust) is removed from the basin center, leaving behind a central mantle (dark gray) zone. Mantle material overlays crustal material further out; this crustal material forms an annulus (ring) of thickened crust in the shallower LTGs, which become less pronounced in the steeper LTGs. Towards the basin edge crustal thickness returns to its pre-impact thickness (50 km).

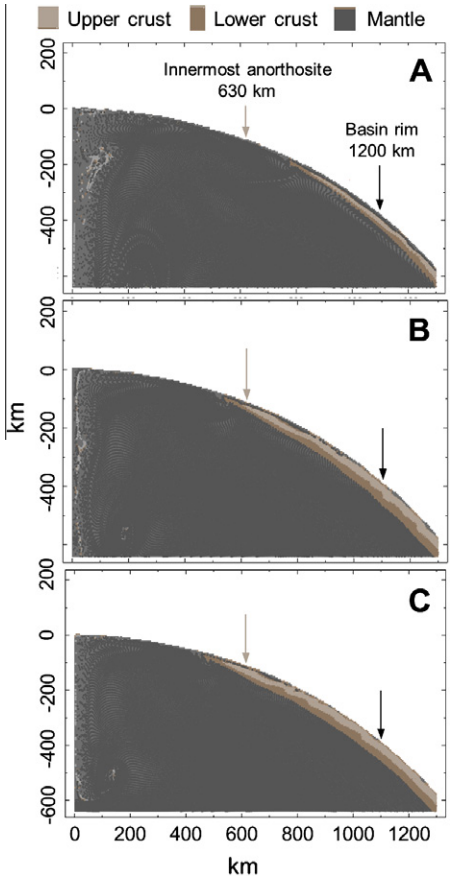

Fig. 8. The effect of impactor size (energy) on basin structure for impactors (A) 250 km, (B) 170 km and (C) 150 km in diameter, traveling at 10 km/s in the steepest LTG. The more energetic the impact, the larger the central mantle (dark gray) zone – crustal material (beige – upper crust; brown – lower crust). Arrows represent the innermost occurrence of anorthosite (Petro and Pieters, 2002) and the basin rim (semimajor axis) (Garrick-Bethell and Zuber, 2009).

also result in a greater volume of melt for a given impact energy as the warmer target requires less energy to melt.

3.4. Final crater structure

The final crustal structure surrounding the basin was also affected by the LTG. Fig. 7 shows impacts into targets with a shallower LTG formed an annulus (ring) of thickened crust at the edge of the central mantle zone, while impacts into the steeper LTGs produced less prominent annuli and a more gradual increase in crustal thickness. (In Figs. 7 and 8 the crust is divided into two layers to represent upper crustal material – initially at depths of 0–25 km – and lower crustal material – initially at depths of 25–50 km. This is done purely to highlight the relative locations of upper and lower crustal material following basin formation; the crust was modeled as a single material in the simulations.) During the impact process, material is initially moved ballistically from the expanding transient cavity; at later stages material location is affected by the collapsing central uplift (see Fig. 2). A cooler and stronger lithosphere inhibits the motion of material following central uplift collapse resulting in the creation of an annulus at the innermost edge of the crustal material in the shallower LTGs. In the example in Fig. 7, the innermost point of crustal material in the shallowest LTG (a) is ~50 km below the surface, however impacts into steeper LTGs, resulted in this innermost crustal point being closer to the surface; in the steepest LTG (c) crustal material is ~10 km below the surface.

Impactor size (energy) also affects the final crustal structure surrounding the basin; Fig. 8 illustrates basins formed in the steepest LTG by projectiles 250, 170, and 150 km in diameter impacting at 10 km/s. The size of the central mantle zone (and therefore the first occurrence of crustal material) increases with increasing energy. The more energetic impacts also excavate and exhume a greater volume of mantle material to the lunar surface to overlay crustal material. For example, the 250 km diameter impactor removes crust far beyond the observed innermost anorthosite signatures and excavates mantle far beyond the observed rim. In contrast, the 150 km diameter impactor results in anorthosite being found closer to the basin than observed, and mantle material being excavated to a smaller radius (830 km) than the observed basin rim (1200 km). A comparison of impact features for impact simulations employing the steepest LTG is given in Table 3.

4. Comparison with observations

4.1. Crustal thickness and topography

Fig. 9 compares gravity-derived crustal profiles beneath SPA to the modeled basin crustal profiles shown in Fig. 7. The gravity-derived profiles suggest the crust beneath the center of SPA has a thickness of ~30–55 km, gradually thickening towards ~60 km nearer the basin's edge (radial distance of ~1200 km). Unlike the majority of gravity-derived crustal profiles for smaller lunar basins, SPA does not appear to possess a thickened annulus of crust around its basin rim (see Wieczorek and Phillips, 1999; Hikida and Wieczorek, 2007; Sasaki et al., 2010, 2011). By comparison to the gravity-derived profiles, our steepest LTG (50 K/km) therefore appears to best fit the gravity data, as the other, shallower, LTGs all produced a prominent thickened annulus.

However our models only cover the first few hours after impact and do not model the post basin-formation modification. Therefore it could be argued that SPA did initially possess a crustal annulus which gradually relaxed over time producing the structure seen today. However, in our models, we found that impacts using the cooler LTGs produced more pronounced crustal annuli than impacts into the warmer LTGs. If SPA did form in a cooler LTG it would have produced less melt and a more pronounced thickened annulus. To match SPA observations today (no noticeable crustal

Table 3
Model data for impactors into the steepest LTG at 10 km/s. D_i: impactor diameter, r_{tc}: transient crater radius. V_m: melt volume. V_{tc}: transient crater volume.

D_i (km)	r_{tc} (km)	V_m (10^8 km^3)	V_{tc} (10^8 km)	V_m/V_{tc}	Innermost norite (km)	Innermost anorthosite (km)	Furthest excavated mantle (km)
250	570	2.25	3.22	0.70	810	890	>1460
200	460	1.10	1.80	0.61	660	730	1460
170	410	0.67	1.17	0.57	550	620	1040
150	360	0.42	0.85	0.50	470	540	830

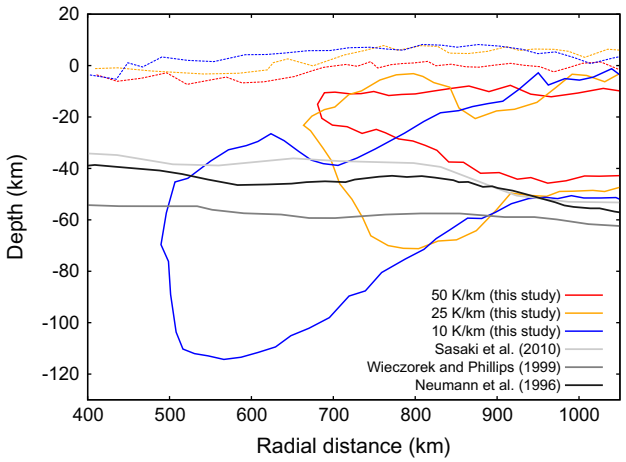

Fig. 9. Cross-sectional crustal thickness profiles for basins formed by a 200 km diameter impactor at 10 km/s into the 10, 25, and 50 K/km LTGs (see Fig. 7 also). Crustal material is absent from the basin center in all our models. The shallower LTGs exhibit a more pronounced thickened crustal annulus. Inferred crustal thicknesses taken from Neuman et al. (1996), Wieczorek and Phillips (1999), and Sasaki et al. (2010), are included for comparison. The rapid change in elevation at the top of crust is a result of the cell size and the spherical nature of the modeled target.

annulus, cool internal temperatures), this basin would have had to relax a greater amount than a corresponding impact into a warmer LTG (which would have produced more melt and a less noticeable crustal annuli); a greater amount of relaxation in cooler post-impact conditions compared to warmer post-impact conditions seems unlikely. Additionally, Mohit and Phillips (2006) investigated visco-elastic relaxation of basin topography for a number of basins, including SPA, concluding that SPA appears to have experienced very little relaxation of its crustal structure since formation. Therefore we believe our comparison using the steepest LTG is justified.

All our models predict the complete removal of crust from the basin center following impact, which is inconsistent with published crustal thicknesses under the SPA basin. As discussed in the Introduction we have assumed for the purposes of this work that this apparent discrepancy between our (as well as previous SPA-scale) models and observations is reconciled by the formation of a new crustal layer of anomalous composition less dense than the mantle, via the cooling, re-crystallization and differentiation of the large central melt pool (Morrison, 1998) present in the basin center in all our simulations. Differentiation would produce an upper layer of noritic composition, which is consistent with spectral analyses of noritic (Pieters et al., 2001) to mafic (Hawke et al., 2003) material. Central peaks of younger craters that reveal deeper levels within the SPA melt pool reveal ultramafic assemblages (Nakamura et al., 2009), further substantiating differentiation of a melt pool with a significant mantle component. The 10–50 km thick layers of mantle material, overlaying crustal material towards the basin rim, may also differentiate, though not on the same scale as the larger mantle melt pool at the basin center. However, as these molten mantle layers decreases in thickness towards the edge of the basin, their volume and thickness may prevent differentiation from taking place.

As a consequence of the high initial thermal gradients and the assumed rheology of the mantle, a volume of mantle melt far exceeding scaling law estimates, and comparable to the transient crater volume, filled the central part of the simulated basins. Because the melt sheet has no strength, the basin center should have a relatively flat floor with little topographic relief. This is seen in Kaguya data where the central region of the basin is at a depth of about 5 km relative to the Moon's mean radius (Sasaki et al., 2010). Beyond about half of the basin radius, the effect of impact heating is minor and would not affect the strength of the crust near the basin rim. Therefore, basin topography at the rim and beyond would be primarily affected by the impact process (e.g. excavation and collapse of the central uplift) rather than by impact heating and melt production. The former would help create and preserve topography, while the latter would tend to flatten any created topography. At the end of the simulations, the deep central melt pool is still hot and hence thermally expanded. Over time, as the melt zone cools, contraction may cause the basin floor to subside substantially, increasing basin depth; combined with the possible differentiation of the melt sheet and any isostatic re-adjustments, this could explain the significant topographic range between the center of the SPA basin and its rim height. Unfortunately, the cell size used in this study (2.5–5 km/cell) implies SPA's height range (~10 km) would at best be covered by a few cells, precluding an accurate assessment of SPA's topography and any other relatively small-scale features such as the basin rim and any ring structures. Free oscillations affecting the lunar surface, also negated any topographic analysis; Ivanov et al. (2010) found these oscillations continued for up to 6 h after SPA-scale impact.

4.2. Geochemical anomaly

Garrick-Bethell and Zuber (2009) defined the edge of the SPA basin with a topographic feature ~2400 km in diameter. This approximately coincides with the edge of the 5 wt.% Fe zone; an outer geochemically anomalous zone enriched in Fe relative to the lunar average but depleted relative to the Fe content in Inner SPA Terrane (Jolliff et al., 2000). In the simulations presented here, mantle material was excavated and/or uplifted to the lunar surface. Mantle material has a higher Fe content than upper crustal anorthositic material and would therefore produce anomalously high Fe content where it covered the surface, relative to pre-impact upper crustal anorthosite. If differentiation of the mantle took place, then minerals such as norite would float to the top; these would also have an Fe content greater than the mafic-poor anorthosites. The extent of mantle material on the lunar surface in the simulations can therefore approximately represent the edge of the SPA basin – the zone in which Fe content would be above the lunar average as a result of excavation and uplift to the lunar surface of originally deeper and denser material. The furthest surficial extent of mantle increased as impactor size (energy) increased; the models suggest impactors greater than 200 km in diameter eject significant volumes of mantle material far beyond the observed basin (and outer geochemical anomaly) radii, whilst the furthest ejected mantle for impactors 150 km in diameter, fell well inside the edge of the basin (and outer geochemical anomaly).

Yamamoto et al. (2010) found exposures of olivine-rich material, which they believe are derived from the upper mantle, in the walls of large craters residing within the rims of many lunar basins (e.g. Schrödinger crater within the main rim of SPA) suggesting basin-forming impacts can excavate mantle material towards their respective rims (which are then later excavated). However, Yamamoto et al. (2010) did not find any olivine-rich exposures in the center of SPA or any other basin. For SPA, they suggest local differentiation in the post-impact melt sheet may have resulted in orthopyroxene overlying the olivine. Orthopyroxene signatures were found by Nakamura et al. (2009) in the center of SPA within a number of craters (Finsen, Antoniadi, Lyman and Bhabha) suggesting, if it was present, an olivine-rich layer may be covered by orthopyroxene, as a result of local differentiation.

Occurrences of anorthositic material have been observed from a radius of 630 km outwards (Petro and Pieters, 2002). This suggests anorthositic material was completely removed from the basin

center and lies buried beneath a more mafic layer between a radius of 630 km and the final crater rim. This buried anorthositic material was then exposed from near-surface locations by energetic enough, younger impacts. For example, Petro and Pieters (2002) found anorthositic signatures in Apollo (diameter = 537 km), Poincare (319 km) and Leibnitz (254 km) craters. Using the scaling relation of Croft (1985) to estimate the transient crater diameter, and assuming excavation depth is one tenth of this diameter, these craters would have excavated material from depths of ~30, ~20, and ~ 16 km, respectively. This is consistent with our model results, which suggest upper crustal material is $\geqslant$ 10 km below the lunar surface at 600–800 km radius. It is also possible that these impacts that revealed pre-impact anorthosite may also have revealed or uplifted (SPA ejected) mantle. Yamamoto et al. (2010); Yamamoto et al. (2012) found a juxtaposition of plagioclase (anorthosite) and olivine (possibly mantle) signatures in Schrödinger basin within SPA. This juxtaposition could therefore be due to the simultaneous excavation of buried (possibly differentiated) SPA ejected mantle material and the underlying pre-impact crustal anorthosite. The studies of Yamamoto et al. (2010) and Yamamoto et al. (2012) show mantle-like signatures are sparse within SPA. They suggest this may be due to the low resolution of the Spectral Profiler onboard Kaguya, ejecta from other large impacts (e.g. Orientale), or a heterogenous distribution of mantle material from the SPA impact (this may be the result of an oblique impact).

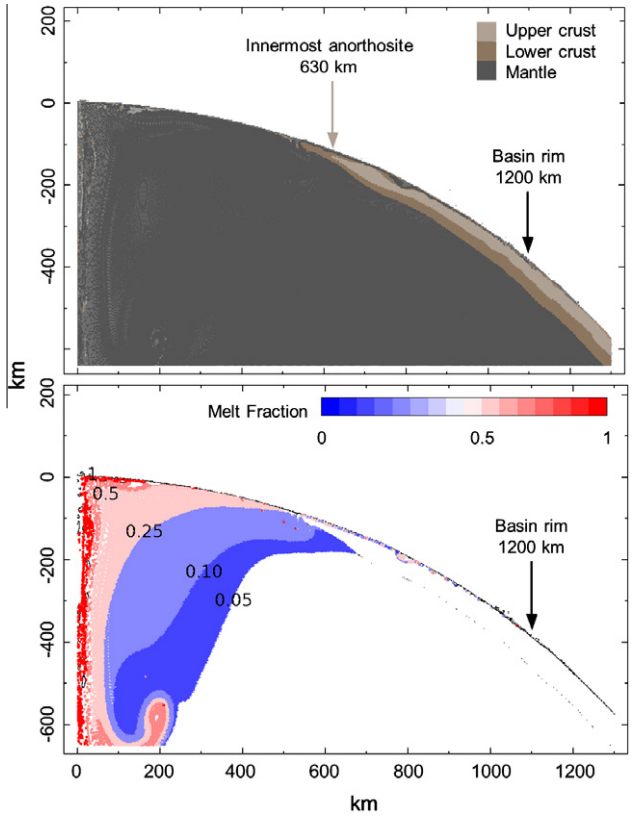

Fig. 10. (Top) Material and (Bottom) melt fraction distribution for the best-fit model using our highest resolution model (34 CPPR, 2.5 km/cell). The innermost occurrence of anorthosite matches extremely well with the observed data, appearing at ~630 km (and initially buried ~14 km below the lunar surface). The outermost occurrence of mantle material at the surface falls short of the observed semimajor axis rim, and the geochemical anomaly, at 1150 km, but has a greater radial distance than the semiminor axis (1000 km). Unmolten mantle material was found excavated to a maximum radial distance of 1210 km, just beyond the basin's semimajor axis.

5. Best-fit model

Comparisons to the observed basin data suggest a 170 km diameter impactor, impacting vertically at a velocity of 10 km/s into the steepest LTG (50 K/km) best estimates the SPA impact. This corresponds to an impact energy of 4×10^{26} J. A different impact scenario (impactor diameter and velocity) with the same impact energy would produce a similar result.

In the best-fit model (Fig. 10), the innermost occurrence of anorthosite was located at a radial distance of 630 km (and buried 14 km below the lunar surface), consistent with observations. Beyond the central molten mantle zone, molten mantle was consistently draped over crustal material forming a layer a few kilometers thick, out to a radial distance of ~900 km, after which exposures became more discontinuous. Molten mantle was located up to a radial distance of 1150 km from the basin center; unmolten mantle was found at the surface out to a distance of 1210 km. As mentioned above, the surficial extent of mantle material can be used to approximate the edge of the basin, based on the observed Fe content; the maximum distance of mantle material matches well with the semiminor and semimajor axis of the observed basin (1000 and 1200 km). The furthest excavated mantle (molten and unmolten) originated from depths of 50 to 80 km, i.e. within the uppermost mantle, the deepest material excavated came from a depth of approximately 100 km. The best-fit model shown in Fig. 10 is a higher resolution model (34 CPPR; 2.5 km/cell) compared to the other models (5 km/cell), however there is good agreement between the two different resolution runs for our best-fit scenario (see Table 2).

At the time of maximum crater volume the cavity was 840 km in diameter. This estimate of the transient crater diameter is far smaller than previous numerical, Hammond et al. (2009) – 2500 km, and observationally-derived estimates: Wieczorek and Phillips (1999) – 2100 km, Spudis (1993) – 1400 km, and Petro and Pieters (2002) – 1260 km. It is also far smaller than the observed final basin diameter (2200–2400 km) and the final crater diameter in the model, which was defined as 2400 km assuming the furthest excavated mantle marks the basin edge. The large ratio of final-to-transient crater diameter is a consequence of extensive collapse of the transient crater, which our models show is highly dependent on the strength of the lithosphere and consequently on the near-surface lunar temperature gradient.

Using our preferred LTG (50 K/km) our best-fit impact scenario produced a mantle melt volume to transient crater volume ratio of 0.55 (mantle melt volume: 6.94×10^7 km^3; transient crater volume: 1.27×10^8 km^3). This value is at least a factor of 3 greater than scaling law estimates, suggesting impacts into pre-heated targets produce a greater volume of melt relative to their transient crater volumes. Our results imply that a transient crater ~2000 km in diameter would produce a volume of melt equivalent to its transient crater volume given our LTGs. According to our simple estimates for our best-fit simulation 3% of the melt was completely molten (had a temperature greater than the liquidus). The basin floor was covered by this completely molten mantle out to a radial distance of ~200 km. ~2% of the total mantle melt volume was located outside of the central mantle zone, overlying crustal material. This mantle material, on average, was cooler than mantle closer to the basin center, with an average melt fraction of ~0.45. The volume of excavated unmolten mantle on the surface equaled 1% of the transient crater volume.

The best-fit model assumed an impact energy of 4×10^{26} J, about an order of magnitude smaller than the estimates of Hammond et al. (2009) and Ivanov et al. (2010). Using an impact energy of 2.5×10^{27} J (velocity 20 km/s; diameter 200 km), Hammond et al. (2009) estimated an excavation depth of 350–380 km, and an excavation cavity of 2500 km; both of these are far bigger than

our model results. However, Hammond et al. (2009) did not consider strength in their model, or use observational data (apart from the observed basin radius) to constrain their results. Ivanov et al. (2010) compared results from a planetary-scale lunar impact simulation (a 300 km diameter impactor, traveling at 18 km/s; energy of 6.58×10^{27} J) to SPA geophysical crustal data of Wieczorek and Phillips (1999). Although they proposed their model was in reasonable agreement with the geophysical data in terms of the location of the thickened annulus of upper crust, their crustal thickness (if equivalent to the inferred upper crust) is far thicker than the inferred total crustal thickness at SPA. Our impact energy estimate is lower than previous estimates because of the hot thermal state of the Moon we assumed as an initial condition. A cooler mantle and less mantle flow over crustal material would allow for larger impact energies (compared to our best-fit energy) to produce basins with features similar to those observed.

6. Consequences of an oblique impact

As SPA is now recognized as an elliptical basin (Garrick-Bethell and Zuber, 2009), it is likely SPA formed by an oblique rather than a vertical impact. The threshold angle (to the target surface) below which a crater with an ellipticity greater than ~1.2 is expected to form depends upon cratering efficiency, the ratio of impactor to transient crater size (Collins et al., 2011). For SPA-scale basins, the threshold angle may be as large as 20–30°. It is possible that the threshold angle may be even larger, if high planetary curvature (the ratio of crater size to planet size) enhances elliptical crater formation, as suggested by the simple geometrical model of Andrews-Hanna and Zuber (2010) and supported by the fact that many other giant impact basins are elliptical, such as Hellas (Andrews-Hanna and Zuber, 2010) and the putative Borealis basins on Mars (Andrews-Hanna et al., 2008; Marinova et al., 2008). However, the giant impact simulations of Marinova et al. (2011) suggest that planetary curvature may not influence crater ellipticity significantly, unless the impact velocity was close to the minimum possible on the Moon.

The asymmetry in thorium and iron concentrations within SPA, with larger anomalies concentrated towards the northwest (see Fig. 2 of Garrick-Bethell and Zuber (2009)), could be due to the asymmetric excavation of an oblique impact, as thorium and iron content are both thought to increase with depth in the Moon (Garrick-Bethell and Zuber, 2009). Schultz (1997) also suggested based on experiments, an oblique (<30°) impact, as well as a low velocity (5 km/s) and large (radius >10% of the lunar radius) impactor. Numerical modeling of oblique SPA impacts by Schultz and Crawford (2011) found impactor decapitation to be prevalent. This resulted in a significant fraction of the impactor being sent into orbit in the Earth–Moon system (as ejection velocity increases with impact obliquity), which could potentially re-impact the Moon. Oblique impacts also result in a decrease in transient crater volume relative to a vertical impact (Pierazzo and Melosh, 2000b).

Impact angle also affects the production of impact melt, focusing melt production downrange, reducing melt volume and depth of melting relative to a vertical impact (Pierazzo and Melosh, 2000b). In a numerical study, Pierazzo and Melosh (2000b) determined that impact melt volume scales approximately with the sine of the impact angle to the target plane. However, Pierazzo and Melosh (2000b) also found the ratio of melt volume to transient crater volume is constant over a wide range of impact angles: 90–30° to the horizontal. In other words, for moderately oblique impacts both impact melt volume and transient crater volume scale as the sine of the impact angle. The numerical simulations of Marinova et al. (2011) also suggest that the ratio of melt volume to crater volume is insensitive to impact angle. Despite the effect of impact angle on various parameters, vertical impacts, such as those carried out in this study, should provide a reasonable qualitative approximation of impacts at 90–30°, but the exact impactor size required to form the SPA basin will depend on the impact angle.

7. Summary and conclusions

The old age, large size and severe degradation of the SPA basin, combined with a lack of direct sampling, means an accurate reconstruction of this basin-forming impact is extremely difficult. Consequently a number of assumptions had to made in this work to be able to constrain a best-fit impact scenario for the SPA basin-forming impact: (1) based on previous models of early lunar evolution, our target had a steep lithospheric thermal gradient and a high internal temperature; (2) we assumed differentiation of the great volume of mantle melt produced in our models could account for the differences in crustal thickness between our simulations (which completely removed the entire crust) and gravity-derived crustal thicknesses around the basin center; and (3) because of resolution limitations we were unable to estimate basin size from a topographic feature, and instead approximated the size of the basin on the extent of exhumed mantle material. Additionally, we included a correction for latent heat in our melt volume calculations, as the ANEOS equation of state tables do not take this into account, to better estimate the actual melt volumes in SPA-scale impacts. Despite our assumptions we can nevertheless draw a number of conclusions about SPA-scale impacts from this work:

1. Excavation depth-to-diameter ratios for SPA-scale impacts remain constant suggesting SPA-scale impacts follow proportional scaling.
2. Inclusion of realistic early lunar thermal gradients, a high internal temperature within the target greatly increases melt volume estimates relative to widely used scaling laws, even with a correction factor for the latent heat of melting taken into account. A consequence is the formation of a deep and broad central melt pool in the basin interior.
3. The initial thermal profile also affects the formation and final structure of the basin. In particular, low lithospheric temperatures encourage the formation of an annulus of significantly thickened crust beneath the outer basin, which is characteristic of impact basins much smaller than SPA. On the other hand, high lithospheric temperatures prevent this annulus from forming.
4. In agreement with previous numerical models, SPA-scale impacts remove the entire crust (given a reasonable pre-impact crustal thickness) from a region around the basin center, exhuming mantle material to the lunar surface (via excavation or the central uplift collapse). To reconcile this prediction with spectroscopic data over the basin center requires the masking of mantle signatures by differentiation of the large central mantle melt pool.
5. A basin producing features similar to those at SPA can be formed by an impactor with an energy of $\sim 4 \times 10^{26}$ J (a dunite impactor 170 km in diameter, traveling at 10 km/s into a target with a 50 K/km lithospheric gradient).

Acknowledgments

R.W.K.P. and G.S.C. are grateful for NLSI travel support allowing them to carry out their research at the LPI-JSC Center for Lunar Science and Exploration, NASA Lunar Science Institute. R.W.K.P. and G.S.C. were both funded by the Natural Environment Research

Council: G.S.C. by NERC Grant NE/E013589/1. W.S.K., P.J.M., and D.A.K. were supported by NASA Cooperative Agreement NNX08AC28A (PI S. Mackwell) and NASA Cooperative Agreement NNA09DB33A (PI D. Kring). We thank Boris Ivanov, Jay Melosh, Kai Wünnemann and Dirk Elbeshausen for their work in the development of iSALE. We also thank an anonymous reviewer and Sarah Stewart for their reviews which helped to improve the clarity and content of this paper.

Appendix A. Supplementary material

videos of some SPA-scale simulations can be found in the supplementary online material (link to Video 1, Video 2 and Video 3) Supplementary data associated with this article can be found, in the online version, at http://dx.doi.org/10.1016/j.icarus.2012.05.032.

References

Amsden, A.A., Ruppel, H.M., Hirt, C.W., 1980. SALE: A Simplified ALE Computer Program for Fluid Flow at all Speeds. Los Alamos National Laboratories Report LA-8095. LANL, Los Alamos, New Mexico. 101pp.

Andrews-Hanna, J.C., Zuber, M.T., 2010. Elliptical craters and basins on the terrestrial planets. In: Gibson, R.L., Reimold, W.U. (Eds.), Large Meteorite Impacts and Planetary Evolution IV. Geol. Soc. Am. Spec. Pap. 465, pp. 1–13.

Andrews-Hanna, J.C., Zuber, M.T., Banerdt, W.B., 2008. The borealis basin and the origin of the martian crustal dichotomy. Nature 453, 1212–1215.

E. Azmon, 1967. The melting of gabbro up to 45 kilobars. NSL, 67–224.

Benz, W., Cameron, A.G.W., Melosh, H.J., 1989. The origin of the Moon and the single-impact hypothesis III. Icarus 81, 113–131.

Cintala, M.J., Grieve, R.A.F., 1998. Scaling impact melting and crater dimensions: Implications for the lunar cratering record. Meteorit. Planet. Sci. 33, 889–912.

Collins, G.S., Melosh, H.J., 2004. Numerical modeling of the South Pole-Aitken impact. Lunar Planet. Sci. 35, 1375 (abstract).

Collins, G.S., Wünnemann, K., 2005. How big was the Chesapeake Bay impact? insight from numerical modeling. Geology 33 (12), 925–928.

Collins, G.S., Melosh, H.J., Morgan, J.V., Warner, M.R., 2002. Hydrocode simulations of Chicxulub crater collapse and peak-ring formation. Icarus 157, 24–33.

Collins, G.S., Melosh, H.J., Ivanov, B.A., 2004. Modeling damage and deformation in impact simulations. Meteorit. Planet. Sci. 39, 217–231.

Collins, G.S., Kenkmann, T., Osinski, G.R., Wünnemann, K., 2008a. Mid-sized complex crater collapse formation in mixed crystalline-sedimentary targets: Insight from modeling and observation. Meteorit. Planet. Sci. 43 (12), 1955–1977.

Collins, G.S. et al., 2008b. Dynamic modeling suggests terrace zone asymmetry in the Chicxulub crater is caused by target heterogeneity. Earth Planet. Sci. Lett. 270, 221–230.

Collins, G.S., Elbeshausen, D., Davison, T.M., Robbins, S.J., Hynek, B.M., 2011. The size–frequency distribution of elliptical impact craters. Earth Planet. Sci. Lett. 310, 1–8.

Croft, S.K., 1980. Cratering flow fields: implications for the excavation and transient expansion stages of crater formation. Proc. Lunar Sci. Conf. 11, 2347–2378.

Croft, S.K., 1985. Scaling laws of complex craters. Proc. Lunar Sci. Conf. 15, C828–C842.

Crosby, A., McKenzie, D., 2005. Measurements of the elastic thickness under ancient lunar terrain. Icarus 173, 100–107.

Davison, T.M., Collins, G.S., Ciesla, F.J., 2010. Numerical modelling of heating in porous planetesimal collisions. Icarus 208, 468–481.

Dence, M.R., 1965. The extraterrestrial origin of canadian craters. Ann. N. Y. Acad. Sci. 123, 941–969.

Garrick-Bethell, I., Zuber, M.T., 2009. Elliptical structure of the lunar South Pole-Aitken Basin. Icarus 204, 399–408.

Ghods, A., Arkani-Hamed, J., 2007. Impact-induced convection as the main mechanism for formation of lunar mare basalts. J. Geophys. Res. 112, E03005.

Grieve, R.A.F., Cintala, M.J., 1992. An analysis of differential impact melt-crater scaling and implications for the terrestrial impact record. Meteoritics 27, 526–538.

Hammond, N.P., Nimmo, F., Korycansky, D., 2009. Hydrocode modeling of the South Pole-Aitken basin forming impact. Lunar Planet. Sci. 40, 1455 (abstract).

Hawke, B.R. et al., 2003. Distribution and modes of occurrence of lunar anorthosite. J. Geophys. Res. 108. http://dx.doi.org/10.1029/2002JE001890.

Hiesinger, H., Head, J.W., 2003. Lunar South Pole-Aitken impact basin: Clementine topography and implications for the interpretation of basin structure and stratigraphy. Vernadsky/Brown Microsymposium 38, MS101 (abstract).

Hikida, H., Wieczorek, M.A., 2007. Crustal thickness of the Moon: New constraints from gravity inversions using polyhedral shape models. Icarus 192, 150–166.

Holsapple, K.A., 1982. A comparison of scaling laws for planetary impact cratering: Experiments, calculations, and theory. Lunar Planet. Sci. 13, 1172 (abstract).

Holsapple, K.A., 1993. The scaling of impact processes in planetary sciences. Annu. Rev. Earth Planet. Sci. 21, 333–373.

Ishihara, Y. et al., 2009. Crustal thickness of the Moon: Implications for farside basin structures. Geophys. Res. Lett. 36. http://dx.doi.org/10.1029/2009GL039708.

Ismail, I.A.H., Murrell, S.A.F., 1990. The effect of confining pressure on stress-drop in compressive rock fracture. Tectonophysics 175, 237–248.

Ivanov, B.A., 2007. Lunar impact basins – Numerical modeling. Lunar Planet. Sci. 38, 2003 (abstract).

Ivanov, B.A., Melosh, H.J., 2003. Impacts do not initiate volcanic eruptions: Eruptions close to the crater. Geology 31, 869–872.

Ivanov, B.A. amd Lagenhorst, F., Deutsch, A., Hornamann, U., 2002. How strong was impact-induced CO_2 degassing in the Cretaceous–Tertiary event? In: Koeberl, C., MacLeod, K.G. (Eds.), Catastrophic Events and Mass Extinctions: Impacts and Beyond. Geol. Soc. Am. Spec. Pap. 356, pp. 587–594.

Ivanov, B.A., Melosh, H.J., Pierazzo, E., 2010. Basin-forming impacts: Reconnaissance modeling. In: Reimold, W.U., Gibson, R.L. (Eds.), Large Meteorite Impacts and Planetary Evolution IV. Geol. Soc. Am. Spec. Pap. 465, pp. 29–49.

Jaeger, J.C., Cook, N.G.W., 1969. Fundamentals of Rock Mechanics. Matheun, London.

Jolliff, B.L., Gillis, J.J., Haskin, L.A., Korotev, R.L., Wieczorek, M.A., 2000. Major lunar crustal Terranes: Surface expressions and crust–mantle origins. J. Geophys. Res. 105, 4197–4216.

Jones, A.P., Price, G.D., Price, N.J., DeCarli, P.S., Clegg, R.A., 2002. Impact induced melting and the development of large igneous provinces. Earth Planet. Sci. Lett. 202, 551–561.

Kiefer, W.S., 2003. Melting in the martian mantle: Shergotite formation and implications for present-day mantle convection on Mars. Meteorit. Planet. Sci. 38, 1815–1832.

Langmuir, C.H., Klein, E.M., Plank, T., 1992. Petrological systematics of mid-ocean ridge basalts: Constraints on melt generation beneath ocean ridges. In: Phipps Morgan, J., Blackman, D.K., Sinton, J.M. (Eds.), Mantle Flow and Melt Generation at Mid-ocean Ridges. American Geophysical Union, Washington, DC, pp. 183–280.

Lawrence, D.J. et al., 2002. Iron abundances on the lunar surface as measured by the Lunar Prospector gamma-ray and neutron spectrometers. J. Geophys. Res. 107 (E12). http://dx.doi.org/10.1029/200JE001530.

Lawrence, D.J., Elphic, R.C., Prettyman, T.H., Gasnault, O., Maurice, S., 2003. Small-area thorium features on the lunar surface. J. Geophys. Res. 108 (E9). http://dx.doi.org/10.1029/2003JE002050.

Lucey, P.G., Taylor, G.J., Hawke, B.R., Spudis, P.D., 1998. FeO and TiO_2 concentrations in the South Pole-Aitken basin: Implications for mantle composition and basin formation. J. Geophys. Res. 103 (E2), 3701–3708.

Marinova, M.M., Aharonson, O., Asphaug, E., 2008. Mega-impact formation of the Mars hemispheric dichotomy. Nature 453, 1216–1219.

Marinova, M.M., Aharonson, O., Asphaug, E., 2011. Geophysical consequences of planetary-scale impacts into a Mars-like target. Icarus 211, 960–985.

Matsumoto, K. et al., 2010. An improved lunar gravity field model from SELENE and historical tracking data: Revealing the farside gravity features. J. Geophys. Res. 115, E06007.

McKenzie, D., Bickle, M.J., 1988. The volume and composition of melt generated by extension of the lithosphere. J. Petrol. 29, 625–679, Part 1.

Melosh, H.J., 1979. Acoustic fluidization: A new geologic process? J. Geophys. Res. 84, 7513–7520.

Melosh, H.J., 1989. Impact Cratering: A Geologic Process. Oxford University Press, New York City, NY.

Melosh, H.J., Ivanov, B., 1999. Impact crater collapse. Annu. Rev. Earth Planet. Sci. 27, 385–415.

Mohit, P.S., Phillips, R.J., 2006. Viscoelastic evolution of lunar multiring basins. J. Geophys. Res. 111, E12001.

Morrison, D.A., 1998. Did a thick South Pole-Aitken basin melt sheet differentiate to form cumulates? Lunar Planet. Sci. Conf. 29, 1657 (abstract).

Nakamura, R. et al., 2009. Ultramafic impact melt sheet beneath the South Pole-Aitken basin on the Moon. Geophys. Res. Lett. 36. http://dx.doi.org/10.1029/2009GL040765.

National Research Council, 2007. The Scientific Context for the Exploration of the Moon. National Academies Press, Washington, DC. 120pp.

Navrotsky, A., 1995. Thermodynamic properties of minerals. In: Ahrens, T.J. (Ed.), Mineral Physics and Crystallography: A Handbook of Physical Constants. American Geophysical Union, Washington, DC, pp. 18–28.

Neuman, G.A., Zuber, M.T., Smith, D.E., Lemoine, F.G., 1996. The lunar crust: Global structure and signature of major basins. J. Geophys. Res. 101, 16841–16863.

Ohnaka, M., 1995. A shear failure strength law of rock in the brittle–plastic transition regime. Geophys. Res. Lett. 22, 25–28.

O'Keefe, J.D., Ahrens, T.J., 1982. The interaction of the Cretaceous/Tertiary extinction bolide with the atmosphere. In: Silver, L.T., Schultz, P.H. (Eds.), Geological Implications of Impacts of Large Asteroids and Comets on the Earth. Geol. Soc. Am. Spec. Pap. 190, pp. 103–120.

O'Keefe, J.D., Ahrens, T.J., 1999. Complex craters: Relationship of stratigraphy and rings to impact conditions. J. Geophys. Res. 104 (E11), 27091–27104.

Onorato, P.I.K., Uhlmann, D.R., Simonds, C.H., 1978. The thermal history of the Manicouagan impact melt sheet, Quebec. J. Geophys. Res. 83, 2789–2798.

Petro, N.E., Pieters, C.M., 2002. The size and location of the transient crater of the South Pole-Aitken Basin. Lunar Planet. Sci. 33, 1848 (abstract).

Pierazzo, E. et al., 2008. Validation of numerical codes for impact and explosion cratering: Impacts on strengthless and metal targets. Meteorit. Planet. Sci. 43 (12), 1917–1938.

Pierazzo, E., Melosh, H.J., 2000a. Hydrocode modeling of oblique impacts: The fate of the projectile. Meteorit. Planet. Sci. 35, 117–130.

Pierazzo, E., Melosh, H.J., 2000b. Melt production in oblique impacts. Icarus 145, 252–261.

Pierazzo, E., Vickery, A.M., Melosh, H.J., 1997. A reevaluation of impact melt production. Icarus 127, 408–423.
Pierazzo, E., Kring, D.A., Melosh, H.J., 1998. Hydrocode simulation of the Chicxulub impact event and the production of climatically active gases. J. Geophys. Res. 103, 28607–28626.
Pieters, C.M., Head, J.W., Gaddis, L., Jolliff, B.L., Duke, M., 2001. Rock types of South Pole-Aitken basin and extent of basaltic volcanism. J. Geophys. Res. – Planet 106, 28001–28022.
Sasaki, S. et al., 2010. Structure of the lunar South Pole-Aitken basin from Kaguya (SELENE) gravity/topography. Lunar Planet. Sci. 41, 1691 (abstract).
Sasaki, S. et al., 2011. Lunar South Pole-Aitken basin from Kaguya (SELENE) gravity/topography. Lunar Planet. Sci. 42, 1893 (abstract).
Schmidt, R.M., Housen, K., 1987. Some recent advances in the scaling of impact and explosion cratering. Int. J. Impact Eng. 5, 543–560.
Schultz, P.H., 1997. Forming the South Pole-Aitken basin; the extreme games. Lunar Planet. Sci. 28, 1787 (abstract).
Schultz, P.H., Crawford, D.A., 2011. Origin of nearside structural and geochemical anomalies on the Moon. In: Ambrose, W.A., Williams, D.A. (Eds.), Recent Advances and Current Research issues in Lunar Stratigraphy. Geol. Soc. Am. Spec. Pap. 477, pp. 141–159.
Shimada, M., Cho, A., Yukutake, H., 1983. Fracture strength of dry silicate rocks at high confining pressures and activity of acoustic emission. Tectonophysics 96, 159–172.
Shoemaker, E.M., 1962. Interpretation of lunar craters. In: Kopal, Z. (Ed.), Physics and Astronomy of the Moon. Academic Press, New York and London, pp. 283–359.
Smith, D.E. et al., 2010. Initial observations from the Lunar Orbiter Laser Altimeter (LOLA). Geophys. Res. Lett. 37. http://dx.doi.org/10.1029/2010GL043751.
Solomon, S.C., Head, J.W., 1980. Lunar mascon basins: Lava filling, tectonics, and evolution of the lithosphere. Rev. Geophys. Space. Phys. 18, 107–141.
Spohn, T., Konrad, W., Breuer, D., Ziethe, R., 2001. The longevity of lunar volcanism: Implications of thermal evolution calculations with 2D and 3D mantle convection models. Icarus 149, 54–65.
Spudis, P.D., 1993. The Geology of Multi-Ring Impact Basins: The Moon and Other Planets. Cambridge University Press, Cambridge.
Stesky, R.M., Brace, W.F., Riley, D.K., Bobin, P.Y., 1974. Friction in faulted rock at high temperature and pressure. Tectonophysics 23, 177–203.
Stewart, S.T., 2011. Impact basin formation: The mantle excavation paradox resolved. Lunar Planet. Sci. 42, 1633 (abstract).
Thompson, S.L., Lauson, H.S., 1972. Improvements in the CHART D Radiation-Hydrodynamic Code III: Revised Analytic Equations of State. Sandia National Laboratory Report SC-RR-71 0714. 113pp.
Tillotson, J.M., 1962. Metallic Equation of State for Hypervelocity Impact. General Atomic Report GA-3216. Advanced Research Project Agency, San Diego. 141pp.
Turtle, E.P. et al., 2005. Impact structures: What does crater diameter mean? In: Kenkmann, T., Hörz, F., Deutsch, A. (Eds.), Large Meteorite Impacts and Planetary Evolution III. Geol. Soc. Am. Spec. Pap. 384, pp. 1–24.
Warren, P.H., Claeys, P., Cedillo-Pardo, E., 1996. Mega-impact melt petrology (Chicxulub, Sudbury, and the Moon): Effects of scale and other factors on potential for fractional crystallization and development of cumulates. In: Ryder, G., Fastovsky, D., Gartner, S. (Eds.), The Cretaceous–Tertiary Event and Other Catatrosphies in Earth History. Geol. Soc. Am. Spec. Pap. 307, pp. 105–124.
Wieczorek, M.A., Phillips, R.J., 1999. Lunar multiring basins and the cratering process. Icarus 139, 246–259.
Wieczorek, M.A. et al., 2006. The construction and structure of the lunar interior. In: Jolliff, B.L., Wieczorek, M.A., Shearer, C.K., Neal, C.R. (Eds.), New Views of the Moon. Mineralogical Society of America, Chantilly, VA, pp. 221–364.
Wünnemann, K., Ivanov, B.A., 2003. Numerical modelling of the impact crater depth-diameter dependence in an acoustically fluidized target. Planet. Space Sci. 51, 831–845.
Wünnemann, K., Morgan, J.V., Jödicke, H., 2005. Is Ries crater typical for its size? An analysis based upon old and new geophysical data and numerical modeling. In: Kenkmann, T., Hörz, F., Deutsch, A. (Eds.), Large Meteorite Impacts and Planetary Evolution III. Geol. Soc. Am. Spec Pap. 384, pp. 514–527.
Wünnemann, K., Collins, G.S., Melosh, H.J., 2006. A strain-based porosity model for use in hydrocode simulations of impacts and implications for transient crater growth in porous targets. Icarus 180, 514–527.
Yamamoto, S. et al., 2010. Possible mantle origin of olivine around lunar impact basins detected by SELENE. Nat. Geosci. 3, 533–536.
Yamamoto, S., Nakamura, R., Matsunaga, T., Ogawa, Y., Ishihara, Y., Morota, T., Hirata, N., Ohtake, M., Hiroi, T., Yokota, Y., Haruyama, J., 2012. Olivine-rich exposures in the South Pole-Aitken Basin. Icarus 218, 331–344.
Ziethe, R., Seiferlin, K., Hiesinger, H., 2009. Duration and extent of lunar volcanism: Comparison of 3d convection models to mare basalt ages. Planet. Space Sci. 57, 784–796.
Zuber, M.T., Smith, D.E., Lemoine, F.G., Neuman, G.A., 1994. The shape and internal structure of the Moon from the Clementine mission. Science 266, 1839–1843.